Magnetic Resonance in Medicine 68:960–968 (2012)

Numerical Simulation of SAR Induced Around Co-Cr-Mo Hip Prostheses In Situ Exposed to RF Fields Associated with 1.5 and 3 T MRI Body Coils

John Powell,[1,2] Annie Papadaki,[1] Jeff Hand,[3]* Alister Hart,[4] and Donald McRobbie[1]

When patients with metallic prosthetic implants undergo an MR procedure, the interaction between the RF field and the prosthetic device may lead to an increase in specific absorption rate (SAR) in tissues surrounding the prosthesis. In this work, the distribution of SAR_{10g} around bilateral CoCrMo alloy hip prostheses in situ in anatomically realistic voxel models of an adult male and female due to RF fields from a generic birdcage coil driven at 64 or 128 MHz are predicted using a time-domain finite integration technique. Results indicate that the spatial distribution and maximum values of SAR_{10g} are dependent on body model, frequency, and the position of the coil relative to the body. Enhancement of SAR_{10g} close to the extremities of a prosthesis is predicted. Values of SAR_{10g} close to the prostheses are compliant with recommended limits if the prostheses are located outside the coil. However, caution is required when the prostheses are within the coil since the predicted SAR_{10g} close to an extremity of a prosthesis exceeds recommended limits when the whole body averaged SAR is 2 W kg^{-1}. Compliance with recommended limits is likely to require a reduction in the time averaged input power. Magn Reson Med 68:960–968, 2012. © 2011 Wiley Periodicals, Inc.

Key words: RF safety; hip prosthesis; local SAR

The use of MRI in patients with orthopaedic implants is increasing, in part due to the number of implants used, and also the realization that metal artefact reduction sequences enable diagnosis of soft tissue problems adjacent to these implants. Further increase is likely due to the predicted increases between 2005 and 2030 of 137 and 601% for total hip and knee replacements, respectively (1). There is also likely to be widespread adoption of 3 T MRI for these patients. During MR procedures involving patients with metallic prosthetic implants, the interaction between the RF field and the prosthetic device may lead to an increase in specific absorption rate (SAR) and consequent tissue heating in areas surrounding the prosthesis. There is uncertainty regarding the degree tissue heating adjacent to metallic implants and a lack of information regarding heating at 3 T compared with that at 1.5 T, or effects associated with bilateral compared with unilateral hip implants. It is important to evaluate the potential increase in the local SAR within this group of patients in terms of SAR and temperature limits stated in standards (2) and safety guidelines (3–5). These are summarized in Table 1. In view of evidence that SAR averaged over 10 g of tissue (SAR_{10g}) has a greater correlation with temperature change than that averaged over 1 g of tissue for several near and far field exposures to frequencies up to 3–6 GHz (6–9), adoption of SAR_{10g} in a recent standard (10), and harmonization in the use of (2), SAR_{10g} is used to describe the local SAR in the work described here.

MRI has been shown to be effective in the management of painful hip arthroplasty (11–13). In practice, pulse sequences such as spin echo (SE) view angle tilting and other metal artifact reduction sequences (14–17) that minimize the artifact caused by the presence of a metallic prosthesis may be used in such clinical procedures. However, there have been relatively few studies of potential RF heating around such prostheses. These include Muranaka et al. (18) who evaluated the temperature rise at locations around the surface of both Cobalt-Chromium (Co-Cr) and Titanium (Ti) hip prostheses contained within a uniform tissue equivalent gel phantom both experimentally and by simulation. The experiments were performed with an average whole body SAR (SAR_{wb}) of 2.5 W kg^{-1} at 1.5 T and a temperature increase as high as 9.0°C was observed around the longitudinal extremities of the prosthesis in the case of a Co-Cr device. Stenschke et al. (19) reported simulations of SAR and temperature on a total hip prosthesis consisting of a Ti shaft and cup with a polyethylene inlay and a stainless steel ball placed in either a rectangular phantom compliant with a ASTM standard (20) or a cylindrical phantom and subjected to RF fields corresponding to 1, 1.5, and 3 T MRI. Results for 1.5 T indicated that a temperature increase of the order of 1°C was induced close to the prosthesis, particularly around the end of the shaft. In a related phantom study that simulated skin contact between thighs (21), temperature increases of ~4.5°C were recorded. Moshin (22) used a finite element method to calculate the electric fields around a Ti steel hip prosthesis implanted in situ in the visible human voxel model due to a 64 MHz birdcage coil. These predictions suggested that regions of increased electric field, and therefore SAR, occurred at the shaft and ball

[1]Radiological Sciences Unit, Charing Cross Hospital, Imperial College Healthcare NHS Trust, London, United Kingdom.

[2]Stroke and Dementia Research Centre, St George's, University of London, London, United Kingdom.

[3]Imaging Sciences Department, MRC Institute of Clinical Sciences, Imperial College London, Hammersmith Hospital Campus, London, United Kingdom.

[4]Department of Musculoskeletal Surgery, Imperial College London, Charing Cross Campus, London, United Kingdom.

*Correspondence to: Prof. Jeff Hand, Ph.D., DSc., Imaging Sciences Dept, Institute of Clinical Sciences, 1st Floor, Neptune Building, Imperial College London (Hammersmith Hospital Campus), Du Cane Road, London W12 0NN, United Kingdom. E-mail: j.hand@imperial.ac.uk

Received 14 July 2011; accepted 1 November 2011.

DOI 10.1002/mrm.23304

Published online 9 December 2011 in Wiley Online Library (wileyonlinelibrary.com).

Table 1
Summary of SAR Limits According to Refs. 2–5. In the Cases of IEC-60601-2-33 and ICNIRP the SAR Limits Over Any 10 s Period Must not Exceed Three Times the Stated Values

Standard or Guideline (reference)	Mass of tissue over which local SAR is averaged (g)	Maximum local SAR (W kg^{-1})		Maximum whole body averaged SAR (W kg^{-1})	Time over which SAR may be averaged
		Trunk	Extremities		
IEC-60601-2-33 (2)	10	10	20	2[a]	6 min
ICNIRP (3-4)	10	10	20	2[a]	6 min
FDA (5)	1	8	12	4	5[b] or 15[c] min

[a]Normal mode.
[b]For local SAR.
[c]For whole body averaged SAR.

extremities of the prosthesis. An increase in temperature of ~1°C after 14 min of RF exposure was predicted in tissue close to the extremity of the shaft.

In the work described here, a commercial electromagnetic field solver software package is used to solve the time-dependent Maxwell's equations and predict SAR distributions, averaged over 10 g of tissue, for the case of bilateral hip implants of Co-Cr-Mo (ASTM F75) prostheses placed in situ within anatomically realistic adult male and female voxel models and exposed to the RF fields from generic birdcage coils driven at 64 and 128 MHz.

METHODS

Whole Body Voxel Models

The voxel models (NORMAN and NAOMI) used in this work were developed by Dimbylow (23,24) and provided by the UK Health Protection Agency under a licensing agreement. These data sets represent a 1.76 m tall male of mass 76 kg and a 1.63 m tall female of mass of 60 kg, respectively, and are comprised of voxels ~2 mm × 2 mm × 2 mm derived from MR acquired data. NORMAN and NAOMI are segmented into 37 and 41 tissue types, respectively. Tissue properties (density, electrical conductivity, and permittivity) used were described previously in Refs. 23–26.

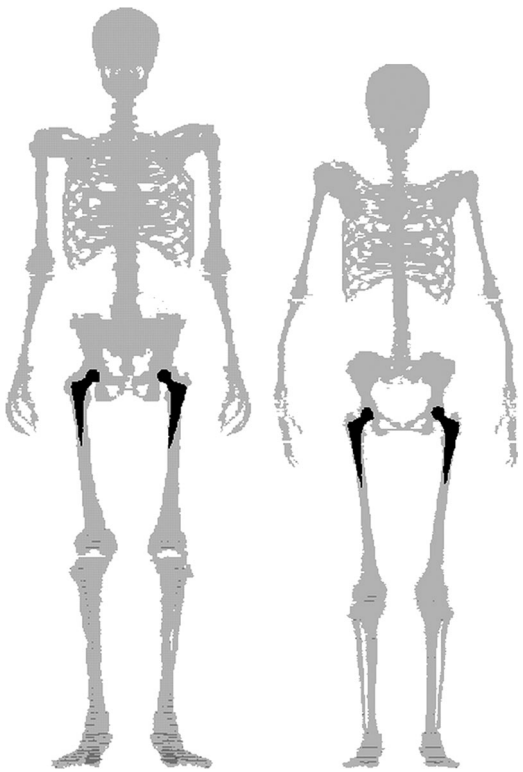

FIG. 1. Prostheses (dark shading) and cortical and trabecular bone in NORMAN (left) and NAOMI (right).

Hip Prostheses

The cemented stem hip prosthesis modelled in this work was made of a nonferrous CoCrMo ASTM F75 alloy with a 150 mm long stem and a semispherical head of diameter 28 mm. The prosthesis was assumed to be homogonous and to consist of its three main composites with relative proportions 61.9% Co, 31.9% Cr, and 7.2% Mo. The overall electrical conductivity (1.44×10^7 S m^{-1}) and density (8455 kg m^{-3}) were calculated by weighting the properties of the individual elements according to these proportions. The magnetic permeability of the prosthesis was 1.00092 H m^{-1} according to the manufacturer (Zimmer Inc., Warsaw, IN).

A CT (Siemens Definition AS64; Siemens Medical Solutions, Erlangen, Germany) acquired volume image of

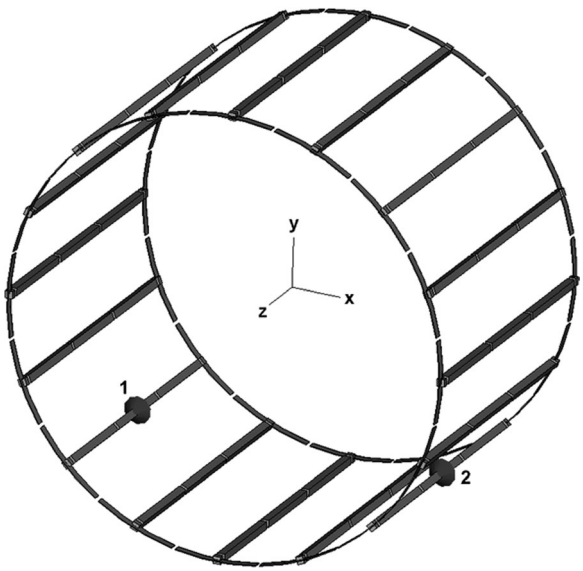

FIG. 2. Birdcage coil showing positions of the two ports (1 and 2). Tuning capacitors are connected across the gaps in the end rings and rungs. The shield is omitted for clarity.

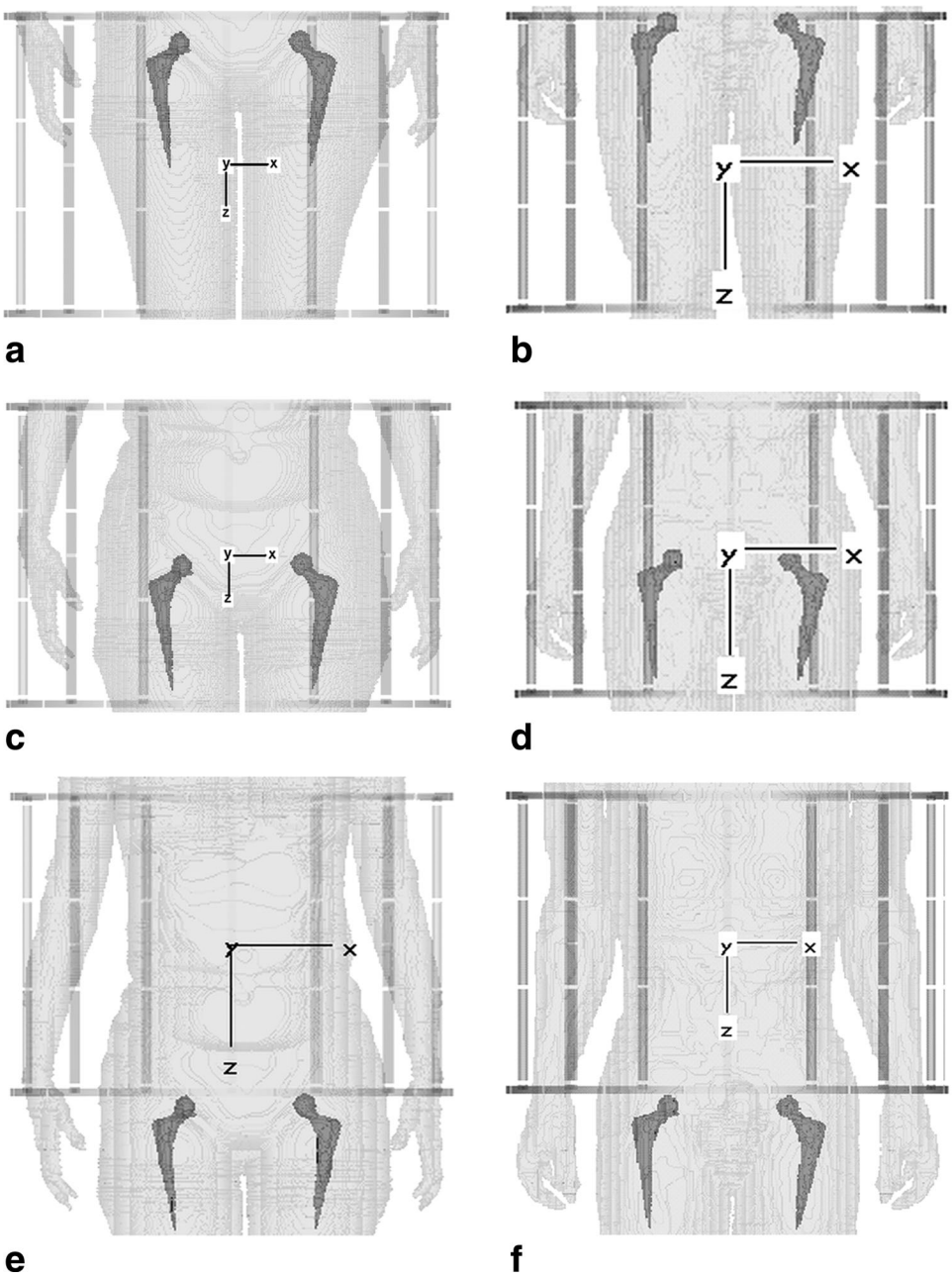

FIG. 3. Positions of bilateral prostheses relative to the center of the coil and coordinate origin for all models studied. Although truncated models are shown here, simulations involved complete NORMAN and NAOMI models (**a**) $NAOMI_{shaft}$; (**b**) $NORMAN_{shaft}$; (**c**) $NAOMI_{ball}$; (**d**) $NORMAN_{ball}$; (**e**) $NAOMI_{out}$; (**f**) $NORMAN_{out}$.

the prosthesis with voxel size $0.6 \times 0.33 \times 0.33$ mm^2 was processed using Analyse v7.0 (AnalyzeDirect Inc., Overland Park, KS) image analysis software to remove image artifacts and to resize the voxels to enable the segmented prosthetic volumes to be reoriented and inserted into the NORMAN and NAOMI models (Fig. 1). The prostheses were inserted realistically into the skeletal structure but because of the postures of the NORMAN and NAOMI models, differences in the y positions between the left and right prostheses were typically in the range 5–10 mm and were dependent on z.

In practice, a gap between the prosthesis and bone is filled with a layer of cement, typically 1–4 mm in thickness. PMMA cement consists of a polymeric powder (polymethylmethacrylate, PMMA) and a monomer liquid part (methylmethacrylate, MMA). After mixing, these fluid substances cure and then set. To assess the effect of the presence of the cement layer, a one voxel thick layer (~2 mm) was added to the surfaces of the prostheses in a modified version of the NORMAN model. The permittivity, conductivity, and density of the cement were taken to be 2.6, 0.003 S m^{-1}, and 1140 kg m^{-3}, respectively.

Numerical Methods

A commercial software package, the Transient Solver within CST Microwave Studio® 2010 (Computer Simulation Technology, Darmstadt, Germany), was used to solve the electromagnetic problem. This provides a solution to the time-dependent Maxwell's equations using a time-domain variant of the finite integration technique described previously in Ref. 27.

Birdcage Coil Models and Simulations

A generic low-pass, 16-rung, shielded circular birdcage coil model provided by a major MR system manufacturer for numerical simulation purposes and previously described by Hand et al. (27,28) was used. The coil was 0.6 m in diameter and the end rings were 10 mm wide with an axial center–center spacing of 0.4 m. The rungs were 10 mm × 10 mm square section rods with their centers located on a circle of radius 0.3 m and the coil was shielded by a 1.0 m long metallic cylinder of thickness 1 mm and internal radius 0.339 m. All coil conductors were assumed to be copper with a conductivity of 5.997×10^7 S m^{-1}. Four capacitors (C_{rung}) were connected across gaps distributed along each rung and 16 capacitors ($C_{\text{end-ring}}$) were inserted in similar gaps in the end rings, midway between rungs.

The complete NORMAN and NAOMI models modified with bilateral prostheses were positioned relative to the birdcage coil such that either the ball or the extremity of the shaft of a prosthesis was located close to the mid ($z = 0$) plane of the coil (referred to as $\text{NORMAN}_{\text{ball}}$/$\text{NAOMI}_{\text{ball}}$ and $\text{NORMAN}_{\text{shaft}}$/$\text{NAOMI}_{\text{shaft}}$, respectively) or the ball end of a prosthesis was located immediately outside the coil (referred to as $\text{NORMAN}_{\text{out}}$/$\text{NAOMI}_{\text{out}}$). Figure 3 shows a truncated view of the relative positions of the prostheses and the coordinate origin located at the center of the coil for all models studied. A coordinate system was defined with its origin at the geometric center of the coil.

The coil loaded with a complete body model was tuned by adjusting the values of $C_{\text{end-ring}}$ and C_{rung} such that the lowest frequency resonant mode occurred at 64 or 128 MHz and was driven in quadrature by two voltage sources located in the rungs at angular positions 135° and 225° relative to the vertical (y) axis (see Fig. 2). No predetermined distribution of currents on the coil conductors was assumed.

The $\pm x$- and $\pm y$-boundaries of the computational domain were positioned 10 mm beyond the radial extent of the RF shield and the $\pm z$ boundaries were positioned ~2 m from the head and feet of the body model. The auto-meshing algorithm within the CST Microwave Studio® transient solver generated nonuniform meshes; minimum mesh steps ranged from ~0.2 mm (128 MHz simulations) and 0.4 mm (64 MHz simulations) up to 40 and 80 mm (for 128 and 64 MHz, respectively) in free space away from structures. NORMAN and NAOMI models consisted of up to $\sim 1.7 \times 10^7$ and $\sim 1.2 \times 10^7$ mesh cells, respectively. All models were excited by a Gaussian pulse ~8 ns (128 MHz) or 16 ns (64 MHz) in duration and simulations ran until the energy within the system decayed to −30 dB relative to its maximum value. This took up to 1400 ns in simulated time. Our previous experience of modelling problems that have analytical solutions and/or comparing solutions obtained using a different solver (e.g., FDTD) suggests that stopping the simulation when the energy within the system has decayed to −30 dB, results in an uncertainty in SAR values of a few (<10)%. This uncertainty can be decreased to ~1% by extending the duration of the simulation and stopping the solver at −40 dB (29). However, in view of other uncertainties inherent in the simulation such as the those concerning the dielectric properties of tissue (30) and the run-time needed in the absence of hardware acceleration, the choice of −30 dB was an acceptable compromise between uncertainty and excessive run-time.

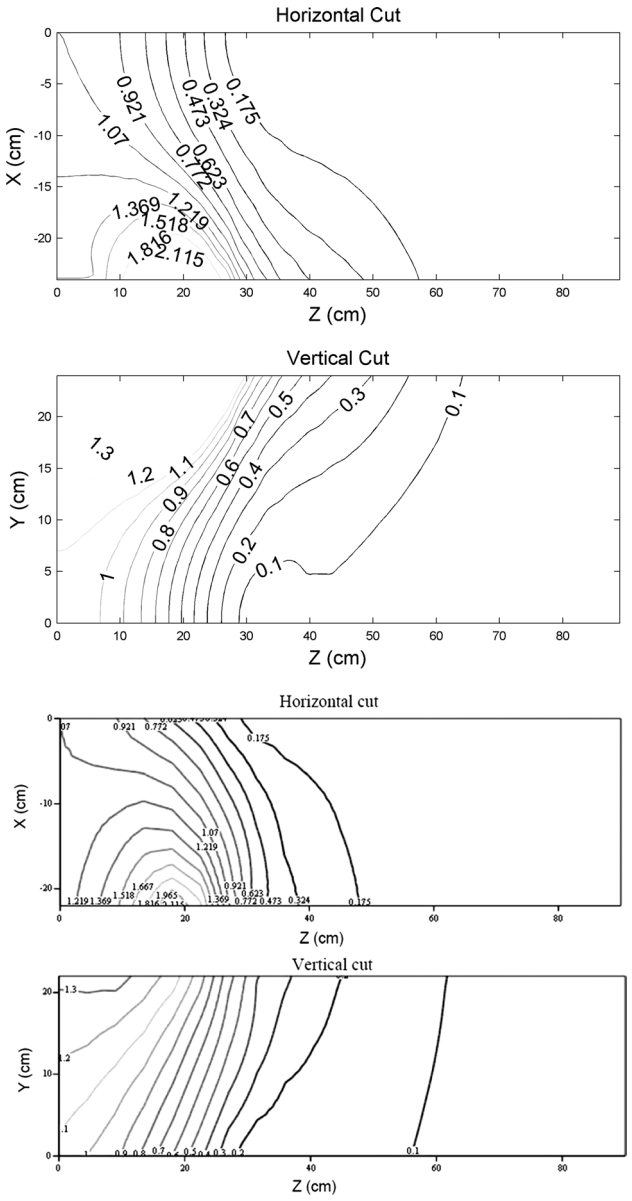

FIG. 4. H-field distributions for 128 MHz birdcage coil. **a**: Simulated distribution in horizontal (y = 0) plane; **b**: simulated distribution in vertical ($x = 0$) plane. **c** and **d** show measured data from within the bore of a 3 T system reported by Capstick et al (29). c: Measured distribution in horizontal ($y = 0$) plane; d: Measured distribution in vertical ($x = 0$) plane. The simulated data are normalized to H(0,0,0) = 1.07 A m^{-1}, the value reported in Ref. 29.

All simulations were run on PCs with 4 Intel Xeon 3.2-GHz CPUs, and 8-GB RAM but without hardware acceleration. In each case the total E- and H-fields, SAR_{wb} and $\text{SAR}_{10\text{g}}$ were calculated. As impedance matching of the coils to a 50-Ω feed was not attempted, field values obtained were normalized to those at the

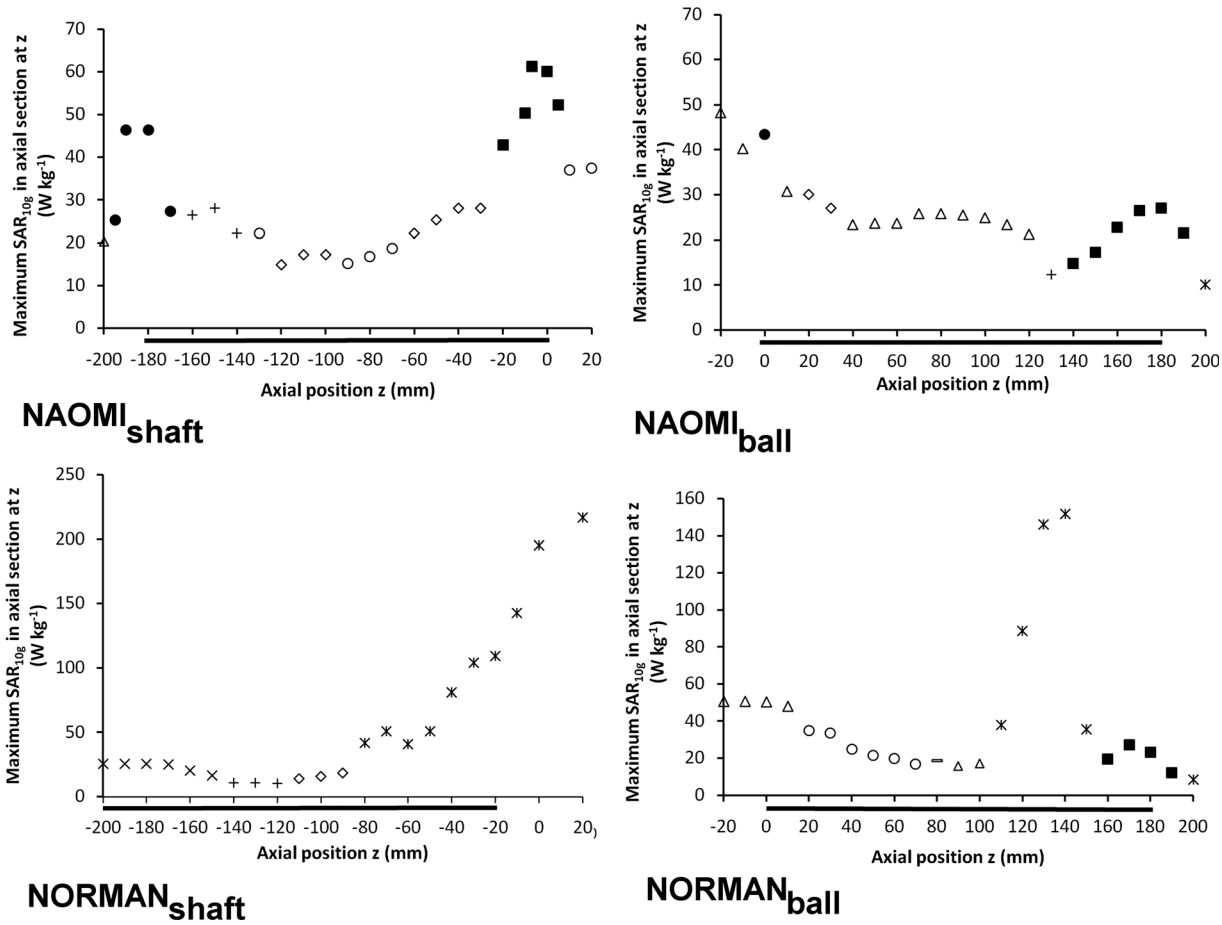

FIG. 5. Location of maximum SAR_{10g} in axial section at z versus axial distance z relative to center of coil. Frequency is 64 MHz. Values are scaled assuming $SAR_{wb} = 2$ W kg^{-1}. Location: △ in arm, wrist or hand; ● at ball end of prosthesis; ■ at shaft end of prosthesis; + posterior right thigh; ○ in anterior right thigh; − in groin; ◇ in posterior left thigh; ∗ in medial left thigh; × intergluteal cleft. The lines beneath the z axes indicate the axial location of the prostheses.

isocenter of the coil and SAR values were scaled assuming the SAR_{wb} was 2 W kg^{-1}.

RESULTS

The simulated H-field distributions due to the 128 MHz coil in horizontal and vertical planes are shown in Fig. 4. Although experimental verification of the predicted H-field was not carried out in this work, measurements made within the bore of a 3 T MR system have been reported by Capstick et al. (31) (Figure 174, p156) and are also shown in Fig. 4 for comparison. The simulated data were normalized to H(0,0,0) = 1.07 A m^{-1}, the value reported in Ref. 31 and are in good agreement with the measured data, which were acquired at 10 or 15 cm spatial increments within the bore of the scanner.

The maximum SAR_{10g} and its location in an axial section at z versus axial distance z relative to the center of the coil over the region containing the prostheses for $NAOMI_{shaft}$, $NAOMI_{ball}$, $NORMAN_{shaft}$, and $NORMAN_{ball}$ is shown in Figs. 5 (for exposure at 64 MHz) and 6 (for exposure at 128 MHz). In all cases the SAR_{10g} values are scaled assuming that SAR_{wb} is 2 W kg^{-1}. Figure 7 shows these data for the cases of $NORMAN_{out}$ and $NAOMI_{out}$ exposed at 128 MHz. Table 2 lists the maximum values of SAR_{10g} located close to a prosthesis and the predicted global maximum SAR_{10g} for each of the six models exposed to both 64 and 128 MHz fields.

In these simulations bone cement, the thickness of which in practice is 1–4 mm and varies from patient to patient, was approximated as trabecular bone. As the conductivity of the cement is significantly lower than that of trabecular bone and its density is greater, this approximation is expected to result in an overestimate of values of SAR_{10g} close to the prostheses, providing a conservative estimate in terms of safety. To confirm this, the simulation of $NORMAN_{shaft}$ at 128 MHz was repeated but with a single voxel layer of cement (∼2-mm thick) added to the surfaces of the prostheses. Peak values of SAR_{10g} close to the prostheses obtained in this simulation showed a decrease of ∼20% compared with the values shown for $NORMAN_{shaft}$ in Fig. 6.

In the cases of $NAOMI_{shaft}$ at both 64 and 128 MHz and $NORMAN_{shaft}$ at 128 MHz, the global maximum SAR_{10g} was located close to the shaft extremity of a prosthesis. In the case of $NORMAN_{shaft}$ at 64 MHz, the maximum SAR_{10g} in the proximity of a prosthesis was also located close to the extremity of the shaft, although the global maximum SAR_{10g} occurred in the skin of the

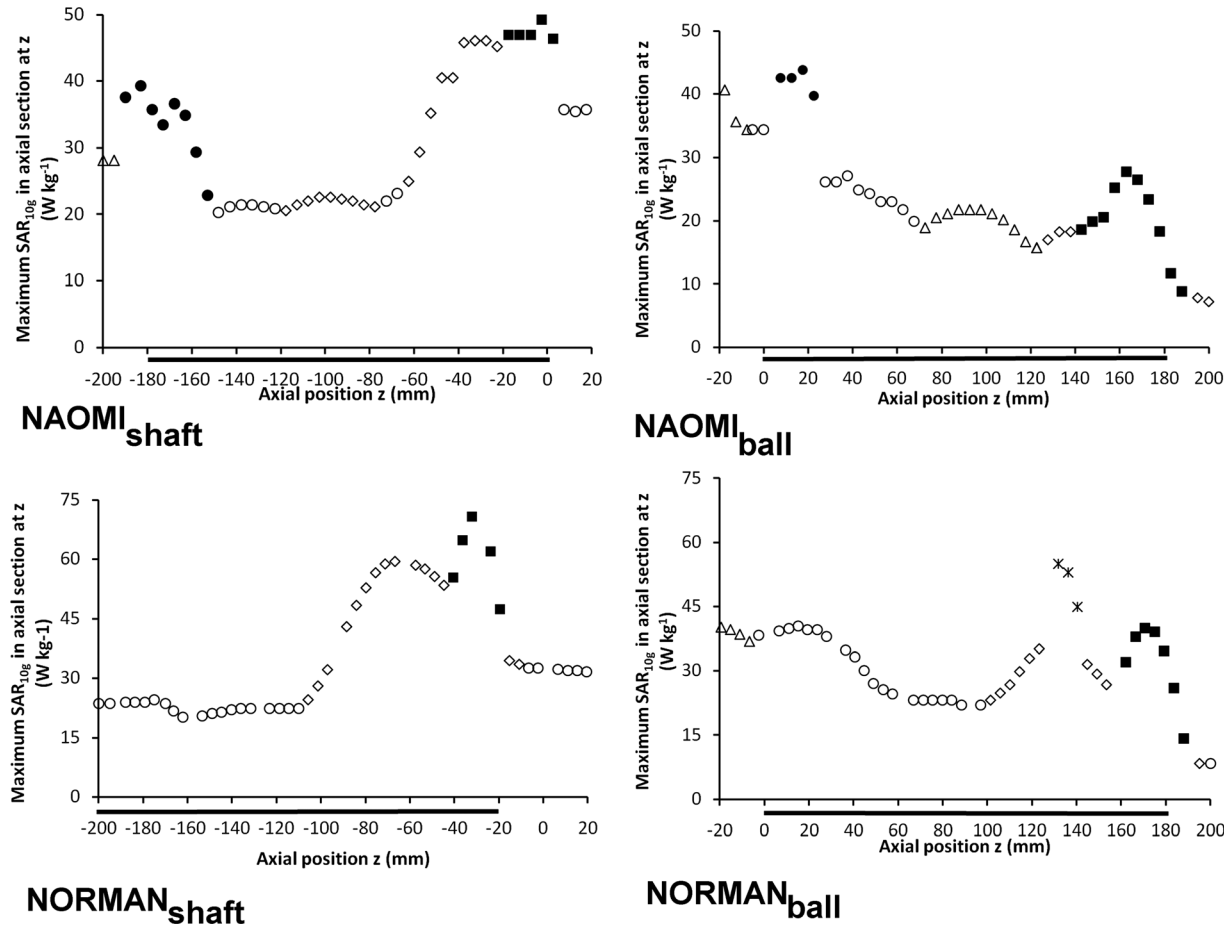

FIG. 6. Location of maximum SAR_{10g} in axial section at z versus axial distance z relative to center of coil. Frequency is 128 MHz. Values are scaled assuming $SAR_{wb} = 2$ W kg^{-1}. Location: △ in arm, wrist or hand; ● at ball end of prosthesis; ■ at shaft end of prosthesis; ○ in anterior right thigh; ◇ in posterior left thigh; ∗ in medial left thigh. The lines beneath the z axes indicate the axial location of the prostheses.

medial left thigh. This was also the case for $NORMAN_{ball}$ at both 64 and 128 MHz. However, for $NAOMI_{ball}$ at both frequencies the maximum SAR_{10g} in the proximity of a prosthesis was located close to the ball extremity of a prosthesis and the global maximum SAR_{10g} occurred in the left arm.

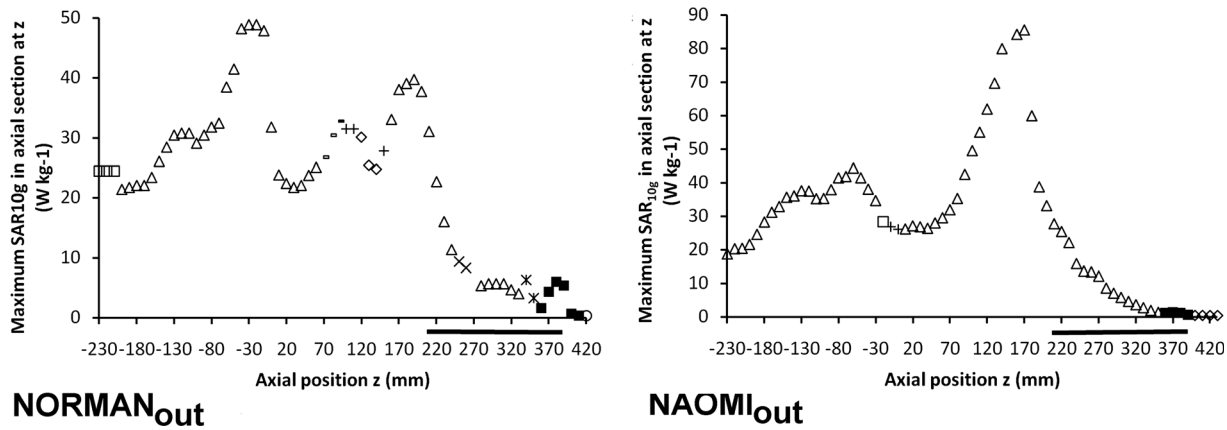

FIG. 7. Location of maximum SAR_{10g} in axial section at z versus axial distance z relative to center of coil for $NORMAN_{out}$ and $NAOMI_{out}$. Frequency is 128 MHz. Values are scaled for $SAR_{wb} = 2$ W kg^{-1}. The end rings of the coil are located at $z = -200$ and $z = 200$ and the lines beneath the z axes indicate the axial location of the prostheses. Location ($NORMAN_{out}$): □ in left shoulder; △ in left arm, wrist or hand; − in skin (left anterior iliac crest); + in skin (sacral region); ◇ subcutaneous (sacral region); × at intergluteal cleft; ∗ in medial left thigh; ■ at shaft end of prosthesis; ○ in skin (anterior left thigh); + skin (sacral region). Location ($NAOMI_{out}$): △ in left arm, wrist or hand; □ in left lumbar region; + in right abdomen; ■ at shaft end of prosthesis; ◇ in left anterior thigh.

Table 2
Maximum Values of SAR_{10g} at a Prosthesis and Global Maximum SAR_{10g} for $NAOMI_{shaft}$, $NAOMI_{ball}$, $NORMAN_{shaft}$, $NORMAN_{ball}$, $NORMAN_{out}$, and $NAOMI_{out}$ Models

	Maximum SAR_{10g} at prosthesis			Global maximum SAR_{10g}		
Model	64 MHz	128 MHz	Location	64 MHz	128 MHz	Location
$NAOMI_{shaft}$	61.3	49.3	Shaft end of prosthesis	61.3	49.3	Shaft end of prosthesis
$NAOMI_{ball}$	43.4	43.9	Ball end of prosthesis	48.3	96.3[a]	Left arm
$NAOMI_{out}$		3	Ball end of prosthesis		90	Left arm
$NORMAN_{shaft}$		72.8	Shaft end of prosthesis		72.8	Shaft end of prosthesis
	38.4		Shaft end of prosthesis	254[b]		Skin of medial left thigh
$NORMAN_{ball}$	27.3	39.9	shaft end of prosthesis	150	55	skin of medial left thigh
$NORMAN_{out}$		6	shaft end of prosthesis		49	Left arm

Values are scaled to $SAR_{wb} = 2$ W kg^{-1} in all cases.
[a]The global maximum SAR_{10g} for $NAOMI_{ball}$ at 128 MHz occurs in the left arm but outside the truncated range shown in Fig. 6.
[b]The global maximum SAR_{10g} for $NORMAN_{shaft}$ at 64 MHz occurs in the skin of the medial left thigh but outside the truncated range shown in Fig. 5.

Figure 8 shows the spatial dependence of SAR_{10g} in coronal planes containing the maximum SAR_{10g} in proximity to a prosthesis for $NAOMI_{shaft}$ due to 64 and 128 MHz fields, $NAOMI_{ball}$ and $NORMAN_{ball}$ due to the 128 MHz field, and $NORMAN_{ball}$ due to 64 and 128 MHz fields. With the exception of $NAOMI_{ball}$, a "hot spot" occurs in the soft tissue inferior to the shaft extremity of a prosthesis. In the case of $NAOMI_{ball}$, the local maximum SAR_{10g} occurs in the soft tissue superior and lateral to the ball extremity. A local increase in SAR_{10g} also occurs in this region in the case of $NAOMI_{shaft}$. Asymmetry in the SAR_{10g} distributions arises from the interaction of the circularly polarized RF fields with the approximately elliptical cross-section of the body (32).

In general, exposure at 128 MHz resulted in a comparable or greater value of SAR_{10g} in the proximity of a prosthesis compared with that at 64 MHz, although $NAOMI_{shaft}$ was an exception in that 64 MHz resulted in a larger SAR_{10g}. Exposure to 64 MHz fields resulted in larger values for the global maximum SAR_{10g} compared with those for 128 MHz in the cases of $NAOMI_{shaft}$, $NORMAN_{shaft}$, and $NORMAN_{ball}$. In contrast, the global maximum SAR_{10g} for $NAOMI_{ball}$ was greater at 128 MHz. By normalizing all values to a SAR_{wb} of 2 W kg^{-1}, recommended limits on SAR_{10g} (see Table 1) were exceeded in all cases in which the prostheses were within the body coil.

When the prostheses were outside the coil, as in $NORMAN_{out}$ and $NAOMI_{out}$, the maximum SAR_{10g} in the proximity of a prosthesis was compliant with recommended limits. Its location was close to a shaft extremity for $NORMAN_{out}$ and close to a ball extremity for $NAOMI_{out}$. In both cases, the global maximum SAR_{10g} was in the left arm and exceeded recommended limits.

DISCUSSION

The results of the numerical simulations described above indicate that the local SAR_{10g} close to a CoCrMo ASTM F75 alloy hip prosthesis in situ in anatomically realistic voxel models of an adult male and female is dependent on the body model, frequency, and position of the prosthesis relative to the transmit coil—in this case, a 16 rung shielded birdcage coil driven at either 64 or 128 MHz. This is in general agreement with previously reported data regarding exposure of other types of hip prostheses exposed to RF fields in 1.5 T systems (19,21,22).

When the prostheses were immediately outside the coil, the maximum SAR_{10g} close to them was compliant with recommended limits. This suggests that it is unlikely that MR procedures involving patients with a CoCrMo ASTM F75 alloy hip prosthesis in which the volume of interest is such that the prosthesis lies outside the birdcage body coil will be associated with significant heating of the implant. On the other hand, when the volume of interest is such that a prosthesis is located within the birdcage body coil, caution is required, because it is likely that local enhancement of SAR_{10g} close to an extremity of the prosthesis will occur. This is particularly so when the extremity of the shaft of the prosthesis is located close to the mid-(axial) plane of the coil. When the ball extremity of the prostheses was located close to the mid-plane of the coil, the location of the predicted maximum SAR_{10g} differed between the male and female models.

In all cases in which the prostheses were within the birdcage coil, values of SAR_{10g} exceeded the limits for normal mode operation of 10 W kg^{-1} (trunk) or 20 W kg^{-1} (extremities) stated in Ref. 2 when SAR_{wb} was 2 W kg^{-1}. The fact that the local SAR limit is exceeded before the whole body SAR limit is reached as been reported in other numerical simulations involving anatomically realistic voxel body models (28,33–35). In the cases of $NAOMI_{ball}$, $NAOMI_{out}$, and $NORMAN_{out}$, the global maximum local SAR_{10g} was in the left arm. In practice, this could be reduced by moving the arms away from the coil. The high global maximum seen in $NORMAN_{ball}$ and $NORMAN_{shaft}$ (at 64 MHz) at the skin of the medial left thigh could be reduced by increasing the gap between the thighs. However, relatively high values of SAR_{10g} ($\approx$27 to $\approx$73 W kg^{-1}) were predicted close to a prosthesis within the coil and to achieve compliance with (time-averaged over 6 min) recommended limits in Refs. 2–4, the time averaged input power would need to be reduced. As was noted earlier, these values are conservative estimates since they were obtained in simulations in which the thin layer of bone cement present in practice was assumed to have the properties of trabecular bone.

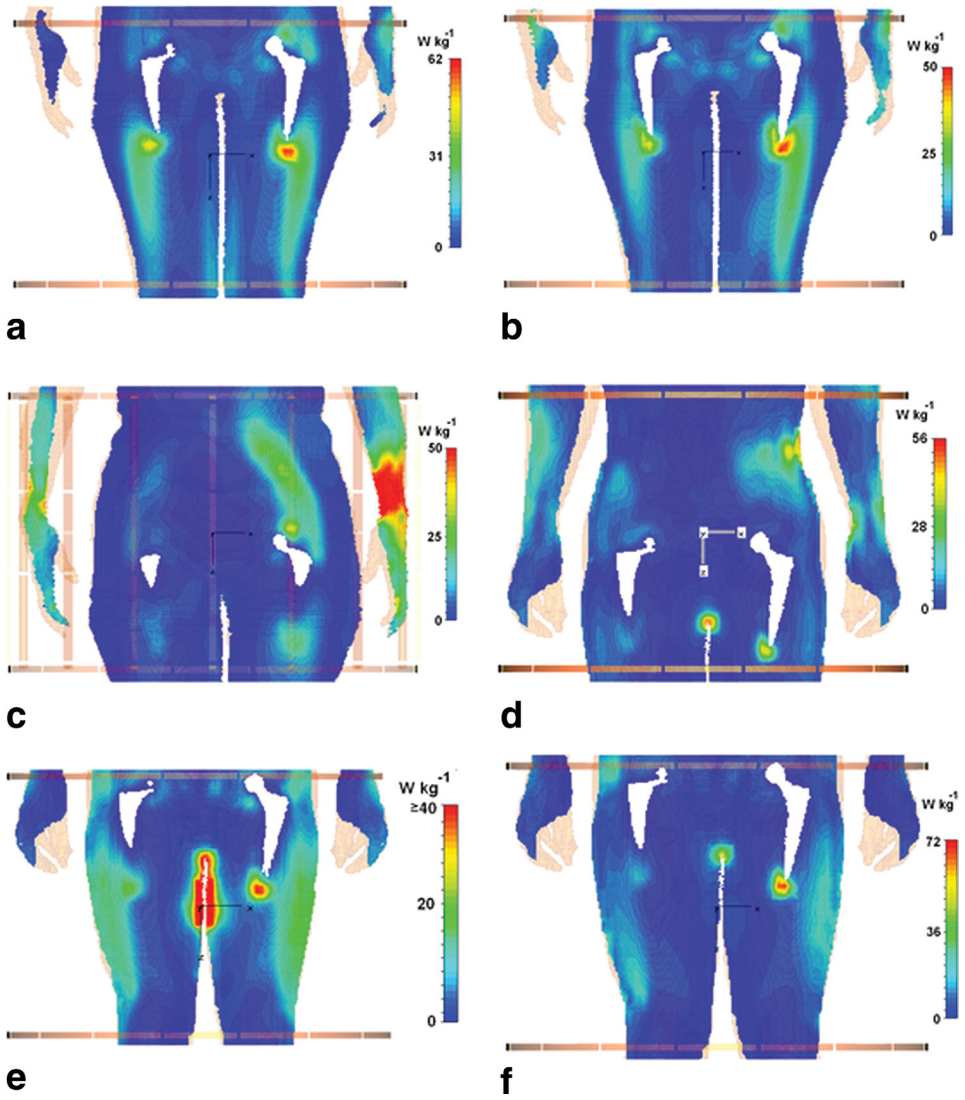

FIG. 8. Spatial variations of SAR_{10g}. The end rings of the coil are shown at top and bottom and the light shading indicates the outline of tissues out of the coronal section. Although truncated models are shown here, simulations involved complete NORMAN and NAOMI models. Top row: $NAOMI_{shaft}$ in planes containing the global maximum values (**a**) 64 MHz - plane $y = -18$ mm, (**b**) 128 MHz - plane $y = -15$ mm; Center row: (**c**) $NAOMI_{ball}$, 128 MHz, plane $y = -30$ mm (**d**) $NORMAN_{ball}$, 128 MHz, plane $y = -26$ mm. In each case the plane contains the maximum SAR_{10g} in proximity to a prosthesis; Bottom row: (**e**) $NORMAN_{shaft}$, 64 MHz, plane $y = -25$ mm containing the maximum SAR_{10g} in the proximity of a prosthesis. (**f**) $NORMAN_{shaft}$, 128 MHz, plane $y = -30$ mm containing the global maximum SAR_{10g}. In (e) the color scale is such that SAR_{10g} values equal to or greater than 40 W kg^{-1} are shown in red. This is to highlight the hot spot close to the prosthesis (39.9 W kg^{-1}); the maximum SAR_{10g} in the groin region is significantly greater than 40 W kg^{-1} (see Table 2).

Although SAR is commonly used in RF safety assessments, it is the combination of excessive temperature and its duration that causes tissue damage. A worst-case estimate of the initial rate of increase in temperature valid only over short times during which there is insignificant heat transfer may be obtained from the relationship $dT/dt = SAR/c$ where c is the specific heat of the tissue. Taking $c = 3500$ J kg^{-1} °C^{-1} (36), the initial dT/dt due to the above range of SAR_{10g} values is approximately 0.008–0.02°C s^{-1}. However, the thermal time constant associated with perfusion effects in tissues is typically 100–200 s (37), and the rate of increase in temperature will be reduced greatly after several minutes of exposure. Nevertheless, temperature increases in excess of 1°C are likely to result from these SAR levels. Greater confidence in assessing the risk of tissue heating around a prosthesis during MR procedures will be gained through detailed thermal modeling.

We have also considered unilateral implants in these models (not reported here) and results suggest that SAR distribution around a single prosthesis is similar to that resulting when it is present as one of the bilateral prostheses. However, the asymmetry in the SAR_{10g} distribution due to the interaction of the circularly polarized RF field with the approximately elliptical cross-section of the body (32) should be considered when assessing the potential heating around a unilateral implant.

Choice of material for the prosthesis is also expected to affect the local SAR and therefore the degree of heating. For example, in comparison with the CoCrMo alloy considered here, a Ti prosthesis has a smaller permeability, a larger specific heat and a smaller thermal conductivity (18). Experimental data in Ref. 18 indicated that a CoCr implant heated more rapidly than a Ti one.

In conclusion, the results of this study suggest that that it is unlikely that significant heating of the implant will occur if the prostheses are located outside the coil. However, when the prostheses are within the coil, caution is required, because the SAR_{10g} close to an extremity of a prosthesis is predicted to exceed recommended local limits when the whole body averaged SAR is 2 W kg^{-1}. Compliance with limits through a reduction in the time averaged input power could present a conflicting requirement with the use of metal artifact reduction sequences, which may utilize shorter B_1 RF pulses but with greater amplitude and consequently higher SAR.

The spatial distribution and maximum values of SAR_{10g} are dependent on body model, frequency and the position of the coil relative to the body.

ACKNOWLEDGMENTS

The authors thank the UK Health Protection Agency for a licensed agreement to use the NORMAN and NAOMI voxel models. Olivia Egan (Chelsea & Westminster Hospital, London) carried out the CT scans.

REFERENCES

1. Kurtz S, Ong K, Lau E, Mowat F, Halpern M. Projections of primary and revision hip and knee arthroplasty in the United States from 2005 to 2030. J Bone Joint Surg A 2007;89:780–784.
2. International Electro-technical Commission (IEC). Medical electrical equipment: Part 2–33. Particular requirements for the safety of magnetic resonance equipment for medical diagnosis. IEC 60601-2-33 ed 2.2. Consolidated with amendments 1 and 2. Geneva: IEC, 2008.
3. International Committee on Non-Ionizing Radiation Protection (ICNIRP).Medical MR procedures: protection of patients. Health Phys 2004;87:197–216.
4. International Committee on Non-Ionizing Radiation Protection (ICNIRP).Amendment to the ICNIRP Statement on medical Magnetic Resonance (MR) procedures: protection of patients. Health Phys 2009;97:259–261.
5. U.S. Food and Drug Administration. Criteria for significant risk investigations of magnetic resonance diagnostic devices. Rockville, MD: Center for Devices and Radiological Health, U.S. Food and Drug Administration, 2003.
6. Fujimoto M, Hirata A, Wang J, Fujiwara O, Shiozawa T. FDTD-derived correlation of maximum temperature increase and peak SAR in child and adult head models due to dipole antenna. IEEE Trans Electromagn Compat 2006;48:240–247.
7. Hirata A, Shirai K, Fujiwara O. On averaging mass of SAR correlating with temperature elevation due to a dipole antenna. Prog Electromagn Res 2008;84:221–237.
8. Razmadze A, Shoshiashvili L, Kakulia D, Zaridze R, Bit-Babik G, Faraone A. Influence of specific absorption rate averaging schemes on correlation between mass-averaged specific absorption rate and temperature rise. Electromagnetics 2009;29:77–90.
9. McIntosh RL, Anderson V. SAR versus VAR, and the size and shape that provide the most appropriate RF exposure metric in the range 0.5-6 GHz. Biolectromagnetics 2011;32:312–321.
10. Institute of Electrical and Electronics Engineers (IEEE) Standard C95.1 2005. Safety Levels with Respect to Human Exposure to Radio Frequency Electromagnetic Fields, 3 kHz to 300 GHz. New York: IEEE, 2006.
11. White LM, Kim JK, Mehta M, Merchant N, Schweitzer ME, Morrison WB, Hutchinson CR, Gross AE. Complications of total hip arthroplasty: MR imaging-initial experience. Radiology 2000;215:254–262.
12. Potter HG, Foo LF, Nestor BJ. What is the role of magnetic resonance imaging in the evaluation of total hip arthroplasty? HSS J 2005;1:89–93.
13. Hart AJ, Satchithananda K, Liddle AD, Sabah SA, McRobbie D, Henckel J, Cobb JP, Skinner JA, Mitchell AW. Pseudotumors in association with well-functioning metal-on-metal hip prostheses. A case-control study using three-dimensional computed tomography and magnetic resonance imaging. J Bone Joint Surgery 2011, in press.
14. Cho ZH, Kim DJ, Kim YK. Total inhomogeneity correction including chemical shifts and susceptibility by view angle tilting. Med Phys 1987;15:7–11.
15. Butts K, Pauly JM, Gold GE. 2005. Reduction of blurring in view angle tilting MRI. Magn Reson Med 2005;53:418–424.
16. Lu W, Pauly KB, Gold GE, Pauly JM, Hargreaves BA. 2009. SEMAC: slice encoding for metal artifact correction in MRI. Magn Reson Med 2009;62:66–76.
17. Koch KM, Lorbiecki JE, Hinks RS, King KF. A multi-spectral three-dimensional acquisition technique for imaging near metal implants. Magn Reson Med 2009;61:381–390.
18. Muranaka H, Horiguchi T, Ueda Y, Usui S, Tanki N, Nakamura O. Evaluation of RF heating on hip joint implant in phantom during MRI examinations. Jpn J Radiol Technol 2010;66:725–733.
19. Stenschke J, Li D, Thomann M, Schaefers G, Zylka W. A numerical investigation of RF heating effect on implants during MRI compared to experimental measurements. Adv Med Eng 2007;114(pt 1): 53–58.
20. American Society of Testing and Materials (ASTM) International. Standard practice for marking medical devices and other items for safety in the magnetic resonance environment. ASTM F2503-05. West Conshohocken, PA: ASTM, 2005.
21. Schaefers G, Kugel H. A basic investigation of heating effects on total hip prostheses in combination with a simulated skin contact of the inner thighs during magnetic resonance imaging (MRI) with an 1.5 Tesla MR system. Proc ISMRM Workshop on MRI Safety: Update, Practical Information and Future Implications, McClean, Virginia, USA, 2005.
22. Moshin SA. Scattering of the magnetic resonance imaging radiofrequency field by implanted medical devices. PhD Thesis, Faculty of Electrical Engineering, University of Engineering and Technology, Lahore, Pakistan, 2008.
23. Dimbylow PJ. FDTD calculations of the whole-body averaged SAR in an anatomically realistic voxel model of the human body from 1 MHz to 1 GHz. Phys Med Biol 1997;42:479–490.
24. Dimbylow PJ. Development of the female voxel phantom, NAOMI, and its application to calculations of induced current densities and electric fields from applied low frequency magnetic and electric fields. Phys Med Biol 2005;50:1047–1070.
25. Gabriel S, Lau RW, Gabriel C. The dielectric properties of biological tissues: 3. Parametric models for the dielectric spectrum of tissues. Phys Med Biol 1996;41:2271–2293.
26. Duck FA. Physical properties of tissue—a comprehensive reference book. London: Academic Press, 1990.
27. Hand JW, Li Y, Thomas EL, Rutherford MA, Hajnal JV. Prediction of specific absorption rate in mother and fetus associated with MRI examinations during pregnancy. Magn Reson Med 2006;55:883–893.
28. Hand JW, Li Y, Hajnal JV. Numerical study of RF exposure and the resulting temperature rise in the foetus during a magnetic resonance procedure. Phys Med Biol 2010;55:913–930.
29. Computer Simulation Technology (CST). Microwave studio workflow and solver overview. Darmstadt: CST, 2007.
30. Hand JW. Modelling the interaction of electromagnetic fields (10 MHz–10 GHz) with the human body: methods and applications. Phys Med Biol 2008;53:R243–R286.
31. Capstick M, McRobbie D, Hand J, Christ A, Kühn S, Hansson Mild K, Cabot E, Li Y, Melzer A, Papadaki A, Prüssmann K, Quest R, Rea M, Ryf S, Oberle M, Kuster N. An investigation into occupational exposure to electromagnetic fields for personnel working with and around medical magnetic resonance imaging equipment. Employment, Social Affairs and Equal Opportunities DG, European Commission, 2008. Available at: http://www.itis.ethz.ch/assets/Downloads/Papers-Reports/Reports/VT2007017FinalReportv04.pdf.
32. Sled JG, Pike GB. Standing-wave and RF penetration artifacts caused by elliptic geometry: an electrodynamic analysis of MRI. IEEE Trans Med Imaging 1998;17:653–662.
33. Collins CM, Mao W, Liu W, Smith MB. Calculated local and average SAR in comparison with regulatory limits. Proc Intl Soc Mag Reson Med 2006;14:2044.
34. Collins CM, Wang Z, Smith MB. A conservative method for ensuring safety within transmit arrays. Proc Intl Soc Mag Reson Med 2007;15: 1092.
35. Wang Z, Lin JC, Mao W, Liu W, Smith MB, Collins CM. SAR and temperature: simulations and comparison to regulatory limits for MRI. J Magn Reson Imaging 2007;26:437–441.
36. Hand JW, Lagendijk JJW, Hajnal JV, Lau RW, Young IR. SAR and temperature changes in the leg due to an RF decoupling coil at frequencies between 64 and 213 MHz. J Magn Reson Imaging 2000;12: 68–74.
37. Foster KR, Lozano-Nieto A, Riu PJ, Ely TS. Heating of tissues by microwaves: a model analysis. Bioelectromagnetics 1998;19:420–428.